AAS 23-148

POST-DOCKING SPACECRAFT DYNAMICS USING MODULAR BAUMGARTE STABILIZATION

João Vaz Carneiro[*], Andrew Morell[*] and Hanspeter Schaub[†]

There are many challenges with spacecraft life extension missions and debris or defunct-satellite removal operations. Physical spacecraft docking has become the dominant approach for many such on-orbit servicing, assembly, and manufacturing (OSAM) missions. The resulting procedures are complex due to the coupled motion between the servicer and target spacecraft. Simulating the physical interactions between multiple satellites is challenging and typically entails developing specific models for the combined servicer with target spacecraft. This process is time-consuming and must be repeated for each mission. This paper proposes a modular approach to accurately describe the dynamics of two spacecraft docked to each other. Taking advantage of classic control techniques, the dynamics of two docked spacecraft, each with its own reaction wheels, flexible solar panels, or sloshing fuel tank structures, can be simulated by numerically enforcing the constraints between these two complex bodies. This numerical approach to model constrained motion between two complex vehicles shows good results suitable for mission analysis, with constraint violations that are multiple orders of magnitude smaller than the size of each spacecraft and the ability to enforce the constraints successfully while applying orbital and attitude maneuvers.

INTRODUCTION

Many spacecraft currently in Earth's orbit have their missions end not due to catastrophic software faults or faulty sensors and instruments but because they run out of fuel to make orbital and attitude corrections. Whether the intention is to remove defunct satellites from orbit or service operational satellites that are running out of fuel, physical spacecraft docking has become the dominantly proposed architecture for doing so. Some of these high-value spacecraft, especially those in geostationary orbit (GEO), are very useful for communications, meteorology, and navigation. Due to their altitude, they are not significantly impacted by atmospheric drag and take a long time to fall into a lower orbit without spending fuel. Extending the operational life of spacecraft already in orbit, especially those occupying important orbits, as well as disposing of defunct satellites, is essential to reducing space-based service costs and minimizing the amount of orbital debris around Earth.

Given these issues and the increased interest in space commercialization, space sustainability has become a major focus of many private companies, and government programs alike.[1] One of the earliest and most extensive examples of on-orbit servicing was the Hubble Space Telescope servicing

---

[*] Graduate Research Assistant, Ann and H.J. Smead Department of Aerospace Engineering Sciences, University of Colorado, Boulder, 431 UCB, Colorado Center for Astrodynamics Research, Boulder, CO, 80309.

[†] Professor and Department Chair, Schaden Leadership Chair, Ann and H.J. Smead Department of Aerospace Engineering Sciences, University of Colorado, Boulder, 431 UCB, Colorado Center for Astrodynamics Research, Boulder, CO, 80309. AAS Fellow, AIAA Fellow.

missions performed by NASA astronauts.[2] On-orbit servicing missions have since changed their focus to robotic solutions. Robotic servicing has been successfully completed by Northrop Grumman's subsidiary SpaceLogistics which started providing life extension for communications satellites in 2020 and 2021 with its Mission Extension Vehicle.[3] Entities currently developing on-orbit servicing technologies include NASA's OSAM-1 mission[4] (previously Restore-L[5]), the European Space Agency's robotic debris removal mission ClearSpace-1,[6] and OrbitFab's Rapid Attachable Fluid Transfer Interface[7] to name a few. Some of these missions focus on removing inactive spacecraft, while others focus on servicing and/or refueling out-of-commission satellites. Besides fixing spacecraft issues, new modules such as a space domain awareness (SDA) sensor can be added to spacecraft to adapt them as technology evolves faster than their orbital lifetime. While they have different mission requirements, all of these scenarios involve a servicer spacecraft reaching a target satellite in orbit and physically docking with it, whether it be to provide a space tug or servicing.

To successfully design such missions, extensive numerical simulation is required to analyze and validate expected mission performance. However, simulating these complex dynamics is far from trivial as each spacecraft can have active attitude control devices, moving hinged solar panels, thrusters, etc. Analytically solving for the post-docking dynamics of each spacecraft is a complex and lengthy process that requires precise knowledge of each spacecraft's components, making it a mission-specific process. Previous work has focused on creating simulations based on actual missions[8,9] by creating a digital twin of the mission hardware. This is expensive and specific to these missions, lacking the generality needed for early-mission design. A common approach is using software packages to simulate these complex dynamics, such as MATLAB[*] and STK[†].

This paper puts forward a general numerical dynamics solution to the problem of two docked spacecraft. Instead of analytically solving for the contribution of each spacecraft on the other, the docking constraint is implemented as a general force and torque to each spacecraft using a numerical proportional-integral-derivative (PID) controller inspired by the Baumgarte stabilization method[10] used in numerical simulation of multi-body systems. Because the constraint is simply applied as a force and torque to each spacecraft, the proposed solution is agnostic to the simulation framework being used. This method has seen specific use in robotics applications, and many papers that study and explore it give robotic arms as an example of a use-case scenario.[11,12] The use of this constraint stabilization method to model docked complex spacecraft has not been considered to date. The kinematic relationship between the two spacecraft is defined through holonomic constraints. Previous work in Ref. 13 focuses on analytically solving for the kinematic relationships between the servicer and the target satellites and then using a second-order sliding mode controller to impose these constraints.

The constraint is implemented in two different simulation frameworks given its framework-agnostic nature. It is first applied in Matlab for testing the method with simplified spacecraft models in a basic orbit before then implementing it with complex spacecraft using the Basilisk Simulation Framework.[14] The Basilisk Simulation Framework's modular approach to dynamics modeling[15] allows for the simple integration of complex simulation tasks, such as fully-coupled attitude control devices[16] or orbital perturbations. Recent work has also introduced a revised architecture that allows multi-spacecraft simulations.[17] The Basilisk Simulation Framework uses the back-substitution method to provide a modular manner to create a large family of single spacecraft dynamics.[15] Subcomponents with their own differential equations, such as reaction wheels or hinged panels, are

---

[*] `https://www.mathworks.com/products/matlab.html`

[†] `https://www.ansys.com/products/missions/ansys-stk`

called state effectors and can be added to the rigid spacecraft hub at run time in a modular manner. However, the current back-substitution method has limits on the topology of effectors that can be added. It is not previously possible to add a complex spacecraft docked to the hub as is now performed by implementing the constraint as a holonomic dynamic effector in Basilisk. Through this the elegant modularity of the back-substitution dynamics is retained, while the holonomic effector allows for 2 or more complex spacecraft systems to be combined into a single dynamical system without having to derive the differential equations of the docked system.

The proposed force and torque solution is general, so it can be applied to multiple scenarios and different connection types. Three different connection types are explored, progressively restricting the system's degrees of freedom. This ensures that the method works for multiple different constraints of increased rigidity. One of the challenges with this approach is that to satisfy the constraints, high gains need to be used for the constraint forces and torques. While the post-docking maneuvers are usually slow to avoid stressing the connections between the servicer and target spacecraft, these high constraint forces and torques lead to very stiff differential equations. Nonetheless, with the appropriate time step and gain selection, the approach is shown to work in various scenarios.

The outcome is a general formulation for the dynamics formulation of two spacecraft docked in orbit, which is applicable to a number of different scenarios. In particular, single-point solutions are avoided, which only apply to a single configuration of docking spacecraft. Rather, the goal is to be able to use two separate spacecraft models, each with complex component dynamics, and enforce docking constraints without having to re-derive problem-specific system equations of motion. Another benefit of this approach is that it yields a time history of the forces and torques needed to satisfy the constraints. When solved analytically, these forces and torques are not directly computed because the constraints are embedded in the equations of motion, and the internal forces and torques do not directly appear. With these, a first-cut approximation of the structural forces and torques can be computed, which is very useful to understand if the two spacecraft can withstand the stresses felt post-docking.

This paper is organized as follows. The problem statement is defined, the general scenario is discussed, and the different constraints are explained. A mathematical overview of the constraint definition is given, along with the method of enforcement through Baumgarte stabilization. Each constraint is then formulated analytically. Finally, a numerical analysis is done, which includes gain analysis, maneuver application, and complex spacecraft analysis.

PROBLEM FORMULATION

This problem formulation aims to be realistic while keeping it general enough to be open to multiple implementations. The general scenario consists of a two-spacecraft configuration after a docking procedure shown in Figure 1. The general spacecraft scenario consists of a two-spacecraft configuration with inertial frame $\mathcal{N}$ at origin N, spacecraft 1's body frame $\mathcal{B}_1$ centered at its center of mass B_1, and spacecraft 2's body frame $\mathcal{B}_2$ centered at its center of mass B_2. Setting the spacecraft's origin at the corresponding center of mass simplifies the equations of motion, as the center of mass is assumed to be constant in the body frame. Spacecraft 1 has mass m_1 and moment of inertia about its center of mass $[I_{1,B_1}]$. Similarly, spacecraft 2 has mass m_2 and moment of inertia $[I_{2,B_2}]$. Spacecraft 1 and 2 each have connection points P_1 and P_2, which are attached by a rigid arm. The connection points are assumed to be fixed to their respective spacecraft hub. Both spacecraft are orbiting Earth in a low Earth orbit (LEO) regime, and each spacecraft is a 6-degree-of-freedom

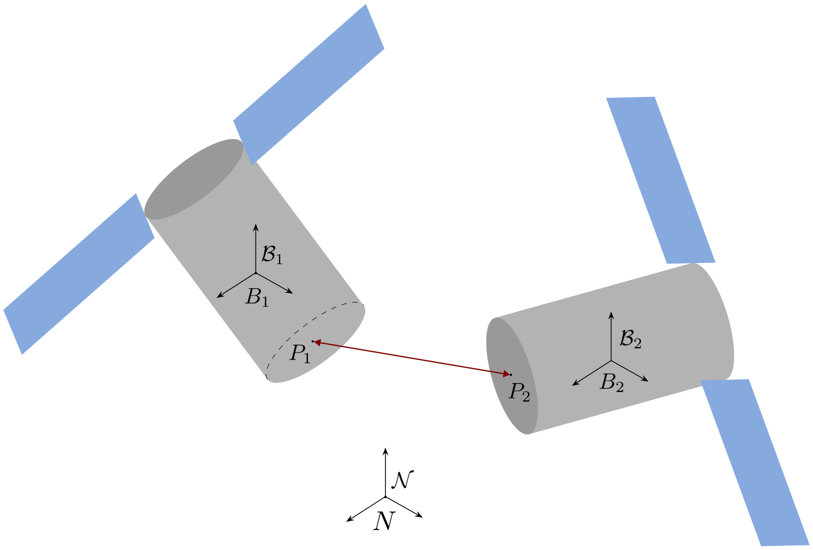

Figure 1: Generalized 6-DOF configuration.

system that includes translation and rotation.

Multiple constraints are studied in this work. The scenarios gradually change from a simple one-degree-of-freedom translation constraint to a full translational and rotational lock between the two bodies. This approach allows the stabilization method to be progressively tested in more constrained scenarios. These tend to be more realistic because, in practice, it is uncommon to have uncontrolled spherical joints in spacecraft operations.

Length Constraint

The length constraint consists of a rigid arm connecting points P_1 and P_2 with a spherical hinge at each end. Both spacecraft must keep a fixed distance l between themselves, although they can rotate about each connection point. This is the simplest translational restriction between two connected bodies, as it is a one-degree-of-freedom constraint. It is enforced by keeping the length of the connecting rigid arm at a fixed length, with no regard for the attitude and angular velocity of each spacecraft.

Direction Constraint

The direction constraint is similar to the length constraint, but spacecraft 1 can no longer rotate about its connection point P_1. In practice, there is now only a single connection point at P_2, and the second spacecraft continues to rotate about it through a spherical hinge. This constraint now locks three-degree-of-freedom and is implemented by setting the direction of $\mathbf{r}_{P_2/P_1}$ fixed in the B_1 frame, where $\mathbf{r}_{P_2/P_1}$ denotes the vector from point P_1 to point P_2.

Rigid Direction Constraint

The rigid direction constraint uses the principles described in the direction constraint but also fixes the second spacecraft's attitude. Therefore, the second spacecraft does not rotate about point P_2. As with the direction constraint, the direction of $\mathbf{r}_{P_2/P_1}$ is fixed in the B_1 frame, with the addition of fixing the rotation of spacecraft 2 about its connection point. This constraint fixes the entire system in place: no translation or rotation is allowed between each spacecraft, which results in a six-degree-of-freedom constraint. The two spacecraft are a single rigid body system with six degrees of freedom (translational and rotational).

MATHEMATICAL OVERVIEW

The holonomic constraint ψ can be defined through a one-dimensional equation that depends on the generalized system coordinates q_i as

$$\psi(q_1, ..., q_n) = 0 \tag{1}$$

These generalized coordinates can be the position, velocity, or attitude components. Each constraint is implemented into the system's equations of motion through a constraint force $\boldsymbol{F}_c$. This force is given by

$$\boldsymbol{F}_c = \lambda \nabla \psi \tag{2}$$

where λ denotes the Lagrange multiplier and ∇ is the spacial derivative operator. The equation above implies that the constraint force is always perpendicular to the constraint surface, which is consistent with physical reality. The constraint force acts on the system to keep the constraint from being violated. Therefore, it will never act on the constraint surface directly, as motion in that surface does not violate the constraint.

Baumgarte Stabilization

Finding the analytic Lagrange multiplier is non-trivial, especially for complex spacecraft systems. Rendezvous, proximity operations, and docking (RPOD) scenarios involve highly coupled dynamics for which solving for the correct Lagrange multiplier is very cumbersome.

The following simple example illustrates why a direct Lagrange multiplier solution is not feasible for docked dynamics of complex spacecraft systems. Take the second time derivative of the constraint ψ and substitute the result into the equations of motion of the system. Let us consider the planar pendulum system to motivate why this is not an appropriate approach. The pendulum's length r is fixed with length l, which means that the constraint is $\psi = r - l$. Taking the second-order time derivative yields $\ddot{\psi} = \ddot{r} = 0$. When implemented numerically, this constraint is affected by numerical instability and finite precision, which means that $\ddot{\psi} = \epsilon \approx 0$, where ϵ is a very small number. While this may not look like an issue, integrating the second-order time derivative yields $\dot{r} = \epsilon t$ and $r = l + \epsilon t^2$. While the value of ϵ can be very small, with enough time, the constraint is bound to be violated above any acceptable threshold.

The Baumgarte stabilization method[10] is used to circumvent these numerical constraint stability issues. This method leverages classic control techniques to simulate constrained dynamics. Instead of solving for the analytic expression of the Lagrange multiplier, a proportional-derivative (PD) controller is used instead, as shown below

$$\lambda = k\psi + c\dot{\psi} \tag{3}$$

where k and c are proportional and derivative gains specified by the user, respectively. This approach ensures that the constraint force is larger when the system is farther away from the constraint surface, going down in value as the system approaches that surface. To allow for perturbation rejection and improve performance, an integral feedback term is included, which yields a slightly modified expression for the Lagrange multiplier as follows

$$\lambda = k\psi + k_{\mathrm{I}} \int \psi + c\dot{\psi} \tag{4}$$

where k_I corresponds to the gain for the integral feedback term $\int \psi$. While ψ and $\dot{\psi}$ can be analytically computed depending on the problem setup, the integral feedback term is always computed numerically by setting its derivative equal to ψ. Therefore, using a PID controller adds as many states as the number of constraints on the system, whereas a PD controller does not need any additional states.

For this method to work, some important considerations must be assessed. The values of the gains c and k must be chosen to be large enough such that the constraints are enforced within a fixed tolerance over a time scale that is smaller than the smallest time scale of the original dynamical system. Aggressive maneuvering can lead to very stiff differential equations. Therefore, a sufficiently small time step of integration is needed to run these simulations, as numerical issues may arise. However, the relative motion of two spacecraft tends to be very slow, so one of the objectives is to understand how well this method can be applied to increasingly complex connected spacecraft systems.

CONSTRAINT FORMULATION

The different constraints must be mathematically defined to implement them into the simulation. It is especially important to be cautious in which frame the constraints are defined and with respect to which frame the constraint derivative is taken. Since both spacecraft are in orbit, in general, the constraints and their derivatives are defined with respect to the body frames as the relative motion between the two spacecraft is being analyzed, not the motion with respect to the inertial frame.

Length Constraint

The length constraint enforces a fixed length between the two connection points P_1 and P_2. Assuming that the constraint length is l, then the constraint is defined as

$$\psi = \|\mathbf{r}_{P_2/P_1}\| - r \tag{5}$$

where r is the rigid arm's length. Since $\mathbf{r}_{P_1/B_1}$ and $\mathbf{r}_{P_2/B_2}$ are constant, then the $\mathbf{r}_{P_2/P_1}$ vector is usually obtained using these two quantities in addition to the inertial position and velocity of each of the spacecraft's center of mass:

$$\mathbf{r}_{P_2/P_1} = \mathbf{r}_{P_2/N} - \mathbf{r}_{P_1/N} = \mathbf{r}_{P_2/B_2} + \mathbf{r}_{B_2/N} - \mathbf{r}_{P_1/B_1} - \mathbf{r}_{B_1/N} \tag{6}$$

The time derivative of the constraint is given by

$$\dot{\psi} = \hat{\mathbf{r}}_{P_2/P_1} \cdot \dot{\mathbf{r}}_{P_2/P_1} \tag{7}$$

where $\hat{\mathbf{r}}_{P_2/P_1}$ corresponds to the unit vector from point P_1 to point P_2 and is given by

$$\hat{\mathbf{r}}_{P_2/P_1} = \frac{\mathbf{r}_{P_2/P_1}}{\|\mathbf{r}_{P_2/P_1}\|} \tag{8}$$

Now that the constraint and constraint rate are analytically defined, the Lagrange multiplier can be computed using either (3) or (4). The gradient of the constraint for spacecraft 1 is $\nabla_1\psi = -\hat{\mathbf{r}}_{P_2/P_1}$

and for spacecraft 2 it is $\nabla_2 \psi = \hat{\mathbf{r}}_{P_2/P_1}$. Therefore, the constraint forces acting on each spacecraft are given by

$$\mathbf{F}_1 = -\lambda \hat{\mathbf{r}}_{P_2/P_1}, \qquad \mathbf{F}_2 = \lambda \hat{\mathbf{r}}_{P_2/P_1} \tag{9}$$

The constraint force acting on spacecraft 1 is equal in magnitude and opposite in direction to the constraint forces acting on spacecraft 2. This is consistent with reality, as when you consider the system of both spacecraft, these are internal forces that should cancel out. It should also be pointed out that the forces act along the rigid arm. Since the goal is to maintain the fixed length of the rigid arm, the constraint forces cannot act in any other direction. If that were the case, the constraint forces would rotate the rigid arm, not acting on the length itself.

It is important to note that because the length constraint only enforces one degree of freedom, each spacecraft is free to rotate about its connection point. Therefore, in addition to the constraint forces applied to each spacecraft at their corresponding connection point, each spacecraft also experiences a torque that arises from the offset between the connection point and the center of mass of each spacecraft as follows

$$\mathbf{L}_{B_1} = \mathbf{r}_{P_1/B_1} \times \mathbf{F}_1, \qquad \mathbf{L}_{B_2} = \mathbf{r}_{P_2/B_2} \times \mathbf{F}_2 \tag{10}$$

Direction Constraint

The direction constraint enforces a fixed direction and length of the connecting arm from spacecraft 1. This means that there are now three one-dimensional constraints defined by

$$\psi_i = \left(\mathbf{r}_{P_2/P_1}\right)_i - (\mathbf{r})_i, \quad i = 1, 2, 3 \tag{11}$$

where **r** denotes the vector that describes the connecting rigid arm, and the i superscript represents the i-th component of the corresponding vector. Because we have three constraints, the translational motion between both spacecraft is locked. The time derivative of each constraint is

$$\dot{\psi}_i = \left(\frac{{}^{\mathcal{B}_1}\mathrm{d}}{\mathrm{d}t}\mathbf{r}_{P_2/P_1}\right)_i, \quad i = 1, 2, 3 \tag{12}$$

The time derivative above is taken with respect to the $\mathcal{B}_1$ frame because the rigid arm should have a fixed direction with respect to spacecraft 1. Since both spacecraft are in orbit, the rigid arm is going to move with respect to the inertial frame. That motion seen by the inertial frame does not necessarily imply a constraint violation. The constraint can be properly analyzed only by taking the time rate of change in the $\mathcal{B}_1$ frame.

The spatial gradient is taken for each scalar constraint to find the constraint forces, which yield three distinct forces. Adding them all up yields a single general constraint for each spacecraft, which is given by

$$\mathbf{F}_1 = \begin{bmatrix} -\lambda^1 \\ -\lambda^2 \\ -\lambda^3 \end{bmatrix}, \qquad \mathbf{F}_2 = \begin{bmatrix} \lambda^1 \\ \lambda^2 \\ \lambda^3 \end{bmatrix} \tag{13}$$

where λ^i corresponds to the Lagrange multiplier from constraint ψ^i. If the constraint and its time derivative are written in a particular frame, so is the constraint force. Again, the forces are equal in magnitude and opposite in direction, canceling out when the system is considered a whole. Since the rigid arm is now fixed at point P_1, the constraint force is applied at point P_2 for both spacecraft. Therefore, the torques experienced by each spacecraft are

$$\mathbf{L}_{B_1} = \mathbf{r}_{P_2/B_1} \times \mathbf{F}_1, \qquad \mathbf{L}_{B_2} = \mathbf{r}_{P_2/B_2} \times \mathbf{F}_2 \tag{14}$$

where $\mathbf{r}_{P_2/B_1} = \mathbf{r}_{P_2/P_1} + \mathbf{r}_{P_1/B_1}$.

Rigid Direction Constraint

The rigid direction constraint builds on top of the direction constraint by locking spacecraft 2 about its connection point P_2. Therefore, we need to define two distinct constraints: ψ_T for the translational constraint and ψ_R for the rotational constraint. The translation constraint is identical to the direction constraint:

$$\psi_T^i = \mathbf{r}^i_{P_2/P_1} - \mathbf{r}^i, \quad i = 1, 2, 3 \tag{15}$$

as is the time derivative:

$$\dot{\psi}_T^i = \left(\frac{^{\mathcal{B}_1}\mathrm{d}}{\mathrm{d}t} \mathbf{r}_{P_2/P_1} \right)^i, \quad i = 1, 2, 3 \tag{16}$$

The constraint forces are:

$$\mathbf{F}_1 = \begin{bmatrix} -\lambda_T^1 \\ -\lambda_T^2 \\ -\lambda_T^3 \end{bmatrix}, \qquad \mathbf{F}_2 = \begin{bmatrix} \lambda_T^1 \\ \lambda_T^2 \\ \lambda_T^3 \end{bmatrix} \tag{17}$$

For the rotational constraint, the relative attitude between both spacecraft is locked, which yields the following formulation:

$$\psi_R^i = \boldsymbol{\sigma}^i_{\mathcal{B}_2/\mathcal{B}_1} - \boldsymbol{\sigma}^i \tag{18}$$

where $\boldsymbol{\sigma}$ is the offset between the two spacecraft written in modified Rodrigues parameters. While this offset is set to zero throughout this work, it can be defined to any value according to the particular implementation. The gradient must be computed to enforce this constraint in attitude space. This yields a torque defined as:

$$\mathbf{L}_c = \begin{bmatrix} -\lambda_R^1 \\ -\lambda_R^2 \\ -\lambda_R^3 \end{bmatrix} \tag{19}$$

where $\lambda_R^i = -k_R \psi_R^i - c_R \dot{\psi}_R^i$. In practice, the formulation used is slightly different than the one used to enforce the translational constraints. $\dot{\boldsymbol{\psi}}_R$ is not used, and the relative angular velocity is used instead. Since each constraint rate is $\dot{\psi}_R^i = \dot{\boldsymbol{\sigma}}^i_{\mathcal{B}_2/\mathcal{B}_1}$, then we can map it into the relative angular velocity as follows

$$\dot{\boldsymbol{\psi}}_R = \dot{\boldsymbol{\sigma}}_{\mathcal{B}_2/\mathcal{B}_1} = \frac{1}{4}[B\left(\boldsymbol{\sigma}_{\mathcal{B}_2/\mathcal{B}_1}\right)]\boldsymbol{\omega}_{\mathcal{B}_2/\mathcal{B}_1} \tag{20}$$

where $\dot{\boldsymbol{\psi}}_R = \left[\dot{\psi}_R^1, \dot{\psi}_R^2, \dot{\psi}_R^3\right]^T$ and $\boldsymbol{\omega}_{\mathcal{B}_2/\mathcal{B}_1}$ is the relative angular velocity between the two spacecraft. This approach is preferable because the angular velocity translates directly into a physical quantity and is one of the system's state variables.

In addition to the constraint forces and torques, the additional torques described in (14) are also present, as the constraint forces are also applied at the point P_2.

NUMERICAL RESULTS

This section shows the corresponding numerical results. These results demonstrate that the stabilization method suits the three constraints described in previous sections. Next, a gain analysis for the PD and PID approaches focuses on the constraint violation performance. This is followed by a runtime analysis to show the feasibility of the method's computational time at varying gains. Next, orbital and attitude maneuver analysis shows that this approach works in more challenging scenarios with dynamic behavior. Finally, the stabilization method is tested within the Basilisk Simulation Framework to validate constraint performance coupled with the dynamic behavior of other on-board components including reaction wheels, solar panels, and fuel slosh.

Constraint Analysis

An initial qualitative assessment of constraint effectiveness can be inferred from observing the relative motion of the two spacecraft. The four points of interest: B_1, B_2, P_1, and P_2 from the configuration shown in Figure 1 are plotted in the $\mathcal{B}_1$ frame for 20 minutes in Figure 2 for each of the different constraint types used.

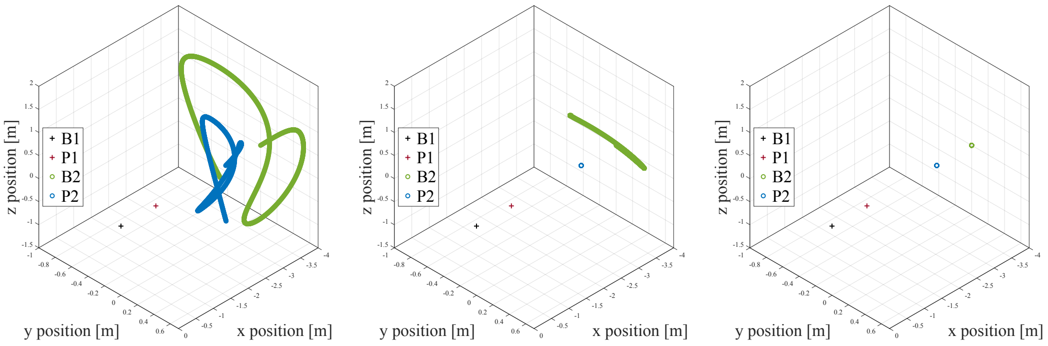

(a) Length Constraint (b) Direction Constraint (c) Rigid Constraint

Figure 2: Relative motion in the $\mathcal{B}_1$ frame for each constraint type.

For all three plots, points B_1 and P_1 stay fixed as is expected considering their fixed definition in the $\mathcal{B}_1$ frame. In Figure 2(a), the relative motion of the length constraint sees P_2 moving on a spherical surface around P_1, and B_2 following at a fixed distance behind P_2. This is consistent with enforcing a fixed distance between P_1 and P_2 without restrictions on either spacecraft's attitude. Figure 2(b) shows P_2 fixed via the direction constraint as is expected by enforcing the direction of P_2 in the $\mathcal{B}_1$ frame. Finally, Figure 2(c) shows all four points of interest fixed in the $\mathcal{B}_1$ frame when enforcing the rigid constraint, as is expected for the additional attitude requirement on $\mathcal{B}_2$ with respect to $\mathcal{B}_1$.

PD Gain Analysis

When using the proportional-derivative (PD) formulation, the gains are represented by proportional gain k and derivative gain c. These gains depend on the Baumgarte stabilization parameters α and β through the following relationships originally used in Baumgarte's stabilization gains.[10]

$$k = \alpha^2, \quad c = 2\beta \tag{21}$$

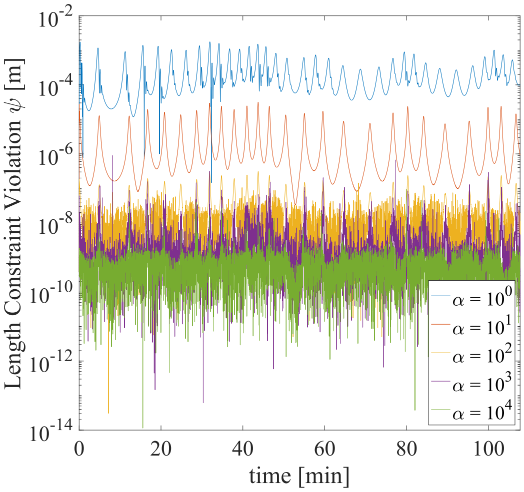

Figure 3: Length constraint violations with the PD formulation.

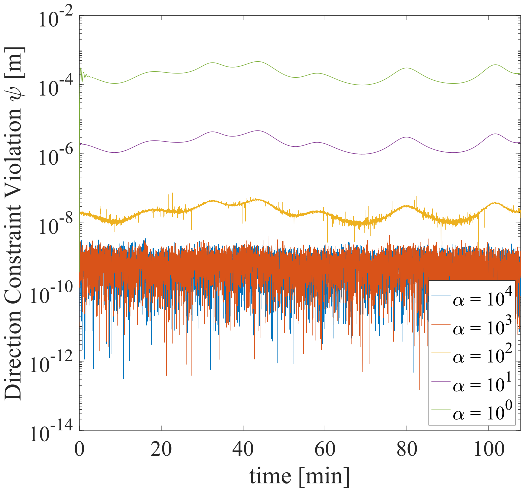

Figure 4: Direction constraint violations with the PD formulation.

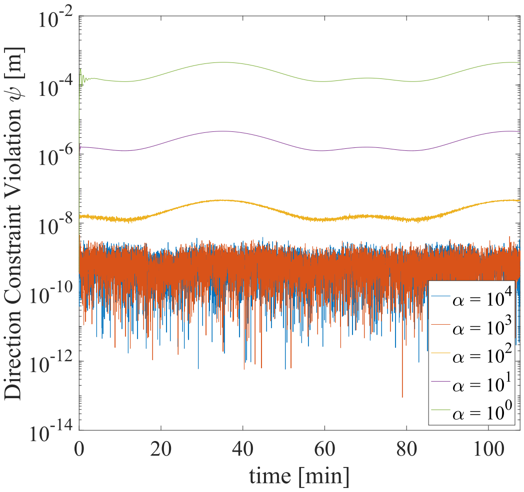

Figure 5: Rigid constraint direction violations with the PD formulation.

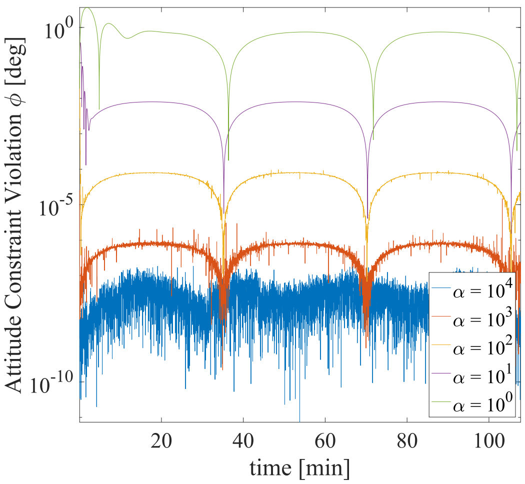

Figure 6: Rigid constraint attitude violations with the PD formulation.

For this work, the parameters α and β are equal, making the simulation parameterized by a single variable. The scenario used for all simulations in the PD and PID gain analyses sets spacecraft 1 as a servicer spacecraft positioned radially on the opposite side from the Earth of target spacecraft 2.

The constraint violations for the length constraint scenario using varying gains are shown in Figure 3. The length constraint violation plot shows that the errors decrease with increasing gains. Assuming a reasonable integration time step, this is expected, as higher gains make the simulation more sensitive to constraint errors. However, these benefits start to plateau for values of α greater than 10^2, and the results become noisier. This can be attributed to a few causes. First, the constraint violations are close to 10^{-10}, approaching the available machine precision. Second, numerical integration also has finite precision, and the propagation errors start to outweigh the benefits of making the dynamics stiffer and more sensitive to constraint violations. Nonetheless, the errors stabilize at 10^{-9} meters, which is more than sufficient for orbital simulations.

The direction constraint uses three one-dimensional constraints to calculate the constraint forces and torques. In order to analyze the constraint violations with a single variable, the norm of the difference between $\mathbf{r}_{P_2/P_1}$ and $\mathbf{r}$ is used, similar to equation (11). This metric includes the direction information, as opposed to the previous metric, which only included the length information. It can be interpreted as an upper bound on the individual constraint violations.

The direction constraint violations for varying gains are shown in Figure 4.Again, the constraint violations are lower for higher gains until they plateau for $\alpha \geq 10^3$, becoming noisier with increased values of α. Finally, the violations settle on the order of 10^{-9}, which is more than adequate for spacecraft simulations. Comparing this Figure 4 with Figure 3, there is an oscillatory behavior in the length constraint scenario that is not present in the direction constraint. This is because the length constraint allows both spacecraft to freely rotate about their hinges, similar to an unstable pendulum. The oscillations are typical of the back-and-forth snapping common to these systems.

For the rigid constraint, there is an additional rotational constraint that needs to be met. The PD gains for the attitude component are calculated using the relationship in (22).

$$k = \left(\frac{\alpha}{10}\right)^2, \quad c = 2\frac{\beta}{10} \tag{22}$$

This relationship between the attitude PD gains and alpha was picked by tuning gain values to minimize attitude constraint violations with $\alpha = 10^2$ held constant. The translation analysis follows the same principles as the direction constraint for the rigid constraint implementation.

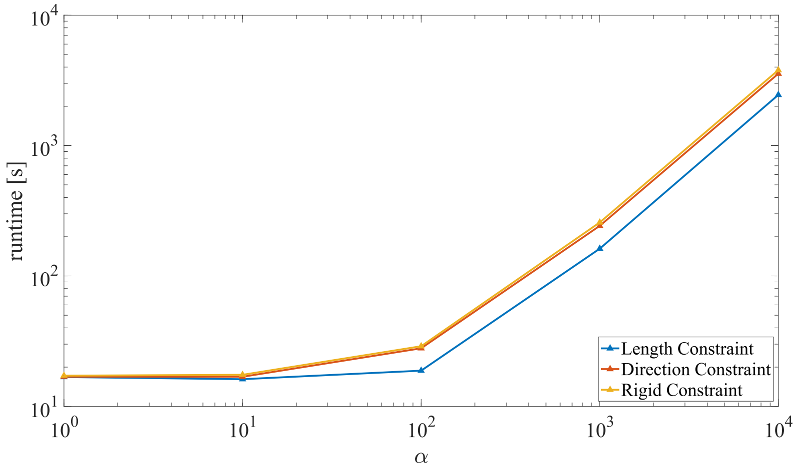

Figure 7: Runtime analysis for all constraint types using the PD formulation.

The direction constraint violations while using the rigid constraint for varying gains are shown in Figure 5, and attitude constraint violations for varying gains are shown in Figure 6. The direction constraint violation results using the rigid constraint are similar to those in Figure 4 from the standalone direction constraint but with a less noticeable oscillatory behavior due to the increased rigidity of this scenario. As for the attitude constraint violations, they are almost constant throughout the simulation except when their value crosses zero at regular intervals (note the logarithmic scale). Following previous trends, the performance increases with higher gains until the results get affected by numerical issues. In this case, the results do not reach a plateau, although it is essential to reiterate that the gains for the attitude constraint are smaller.

While constraint performance is the key metric to understanding whether the proposed method works, it does not tell the whole story. For the approach to be practical, the run time has to be reasonable; otherwise, each simulation takes too long and becomes inappropriate for mission analysis. To that end, the runtimes for each test in the PD gain analysis are shown in Figure 7. The larger the gains, the longer the simulation takes to run. As α increases, the PD gains increase, increasing the constraint forces and causing the Runge–Kutta–Fehlberg (RKF45) integrator to take smaller integration time steps. This happens because the RKF45 integrator uses variable time steps, so the length of simulation time grows dependent on the stiffness of the equations of motion: the stiffer the system, the smaller the integration steps.

PID Gain Analysis

In the PID gain analysis, the proportional and derivative gains for each type of constraint are formulated similarly from parameters α and β as in the PD gain analysis. The integral gain k_I is set to be one order of magnitude smaller than the corresponding proportional gain for each constraint. This relationship between k and k_I was selected from tuning the PID gains to minimize the constraint violations with $\alpha = 10^2$ held constant. The analysis focuses on the same goals of constraint performance and simulation runtime.

The length constraint violations for this formulation are shown in Figure 8. Following the same trend observed with the PD formulation, the constraint violations, on average, decrease as alpha increases. Also similar to the results using the length constraint with the PD formulation, there is oscillatory motion caused by the unstable pendulum-type motion of each spacecraft on the ends of the fixed length snapping back and forth when perturbed by the constraint force. These resulting oscillations in constraint violations show a more considerable peak-to-trough difference in magnitude than was produced using the PD formulation, as the integral gain contributed to larger constraint forces. This also produced a lower average violation using PID compared to PD results at each value of α but plateaued at the same order of magnitude around 10^{-9} meters via the same machine precision and integration limits as was observed in the PD gain analysis.

The direction constraint violations using the direction constraint for varying PID gains are shown in Figure 9. Consistent with previous results, the constraint violations decreased, and high-frequency noise increased with increasing values of α. However, this time the violations reached the plateau limit at $\alpha \geq 10^2$, an order of magnitude lower value for alpha than when the PD formulation reached the plateau. The oscillatory motion is also significantly smaller than observed with the PD formulation, except $\alpha = 10^1$. While it is unclear why this happens for this specific value, it might be because some fundamental modes are excited at just the right frequency by the constraint forces and torques.

The direction and attitude constraint violations for the rigid constraint implementation for varying PID gains are shown in Figures 10 and 11, respectively. Using the rigid constraint, results were again consistent with decreasing constraint violations and increasing high-frequency noise as alpha increased. As the other PID formulation results exhibited, the plateau is reached sooner than the corresponding PD performance in Figures 5 and 6. An interesting behavior arises for smaller values of α, which showed more significant attitude constraint violations at $\alpha \leq 10^1$ compared to the

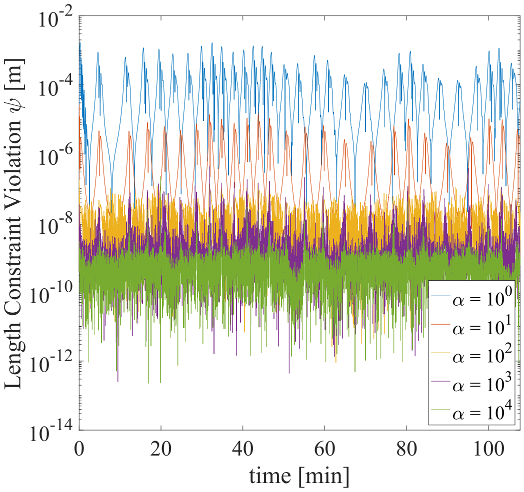

Figure 8: Length constraint violations with the PID formulation.

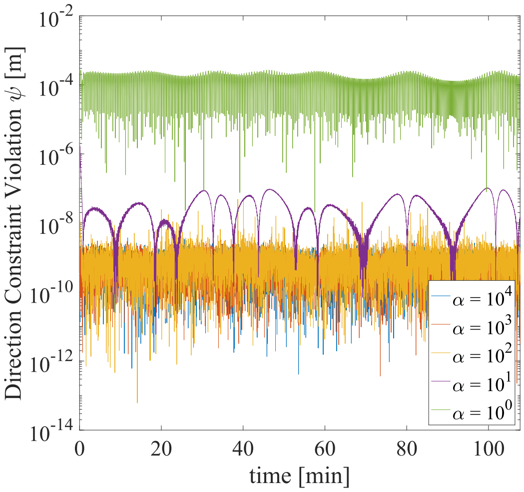

Figure 9: Direction constraint violations with the PID formulation.

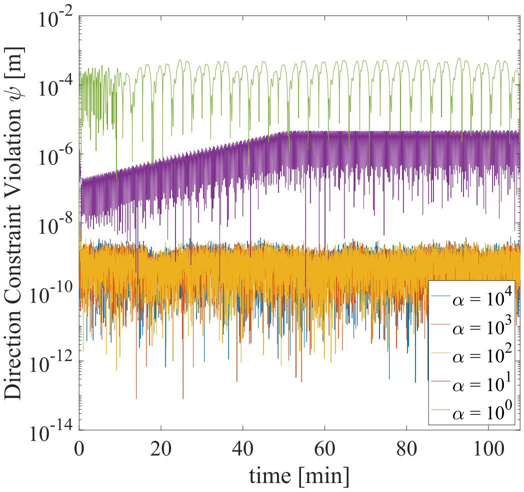

Figure 10: Rigid constraint direction violations with the PID formulation.

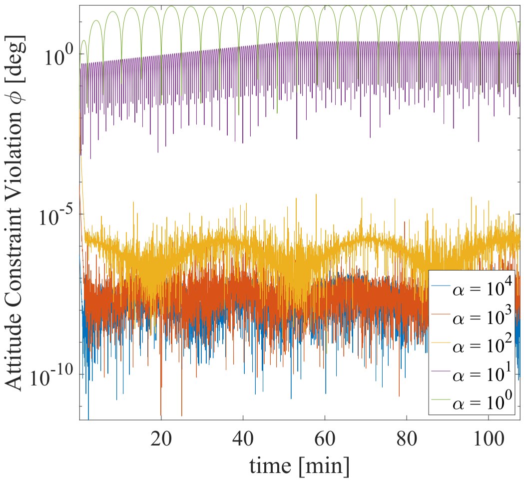

Figure 11: Rigid constraint attitude violations with the PID formulation.

PD formulation. This can be attributed to the fact that lower gains do not adequately enforce the constraints. Adding another feedback term in the form of an integral term only makes that sensitivity more noticeable.

The runtime results are shown in Figure 12 for the PID formulation. As seen in the PD formulation, the runtime increases with increasing α, except for the lowest α tested. This is because sufficiently small PD gains allow more significant constraint violations, increasing the constraint force and driving the RKF45 to smaller time steps. It should be noted that while the runtimes at each α using either the PID or PD formulations are almost identical, the constraint violation magnitudes for the PID formulation are significantly smaller for each constraint type. This shows that the addition of integral gain improves the performance of the constraint enforcement without simply

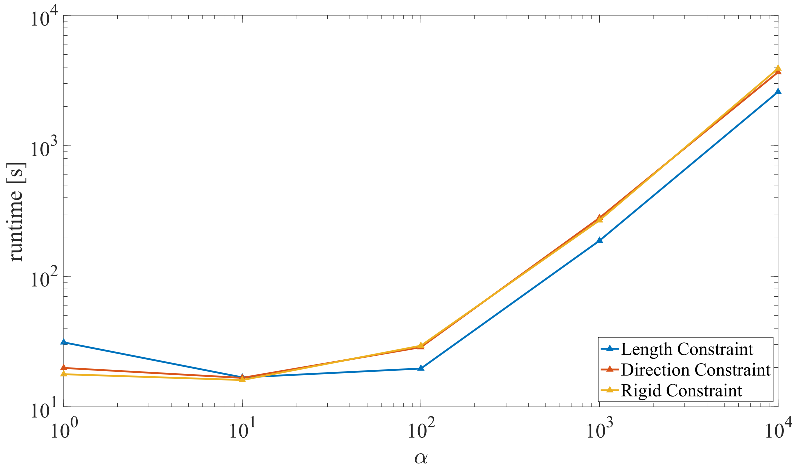

Figure 12: Runtime analysis for all constraint types using the PID formulation.

contributing a larger constraint forces. If this were the case, the larger constraint forces would have made a stiffer dynamical system resulting in longer runtimes.

Maneuver Analysis

While analysis with varying sets of PD and PID gains shows that the method is effective and can yield adequate performance for the right gains, it has only considered the slow motion of a nadir-pointing orbit. While this is an appropriate scenario for initial validation, it does not stress-test the proposed approach for more demanding scenarios such as when the spacecraft are maneuvering together. Therefore, the next step to assess performance is applying perturbations that stress the constraints. For this set of tests, the rigid constraint is selected using all proportional, derivative, and integral gains. It appropriately models a singular rigid robotic arm while also producing the lowest constraint violations in the previous gain analysis. Both maneuvers are performed by only applying forces or torques to the servicer spacecraft, assuming a scenario in which the target spacecraft does not contribute control and the arm between them is therefore stressed greater than if the target spacecraft was cooperative.

Orbital Maneuver The orbital maneuver adds a translational perturbation by applying a force on the servicer spacecraft in the radial direction defined by the Hill frame for spacecraft 1. The force, which simulates low-thrust electric propulsion, is turned on at minute 5 and lasts one minute. The resulting performance of the rigid constraint using the PID constraint formulation with this orbital maneuver is shown in Figures 13 and 14.

Before the orbital maneuver is commanded at minute 5, the constraint violations are consistent with the PID gain analysis results. As the perturbing force is applied, a constraint violation spike occurs, which is smaller for larger values of α. Another smaller spike in constraint violation occurs when the perturbing force is turned off at minute 6, caused by a lag in the contribution from the integral gain. During the maneuver, the constraint violations hover at a value greater than their pre-maneuver value as the system goes through a dynamic simulation phase. After the maneuver is turned off, the constraint violations settle to a lower value.

It should be noted that the steady-state constraint violations after the maneuver are not as low as pre-maneuver magnitudes. This is caused by the residual motion of the joint spacecraft system stressing the constraints slightly more than the slower-moving pre-maneuver joint system. New angular and translational rates of the attached spacecraft characterize this motion. Whereas the slow orbital motion in the PID gain analysis sees a plateau in direction constraint violations at $\alpha \geq 10^1$, for the maneuver scenario, this plateau is only reached at $\alpha = 10^4$. For the attitude constraint violations, this plateau still isn't reached at $\alpha = 10^4$ after the maneuver finishes.

These results show that the method can handle more realistic dynamic scenarios. While the constraint violations increase when the servicer is thrusting, the constraints are still met within reasonable accuracy, and the system can settle after the maneuver is done.

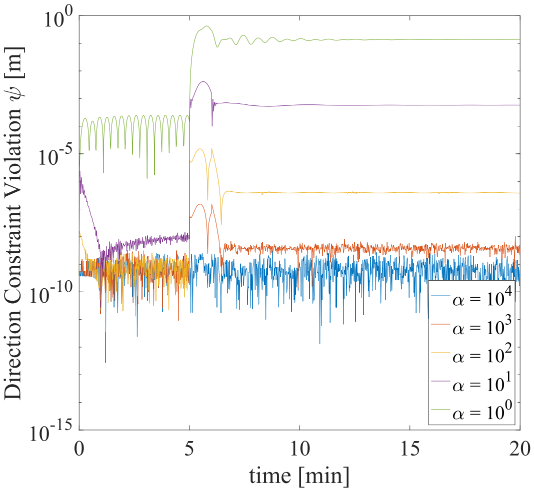

Figure 13: Rigid constraint direction violations with the translational maneuver.

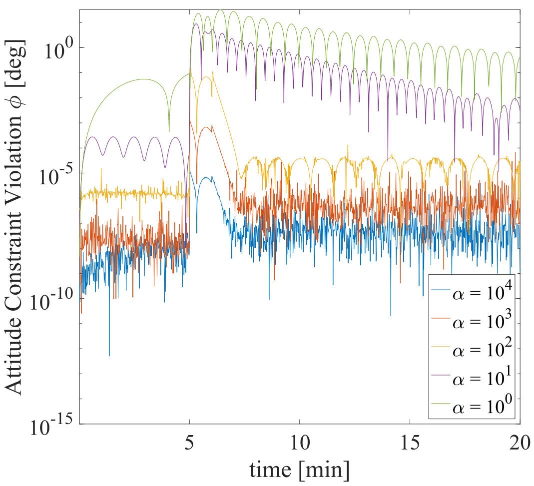

Figure 14: Rigid constraint attitude violations with the translational maneuver.

Attitude Maneuver The second test performs an attitude maneuver, applying a torque to the servicer spacecraft starting at minute 5 until it rotates it by 22.5°. The resulting performance of the rigid constraint using the PID constraint formulation for the attitude maneuver is shown in Figures 15 and 16. Before the rotational maneuver is applied at minute 5, the constraint violations are consistent with the PID gain analysis results. As with the orbital maneuver, there is a constraint violation spike when the control torque is commanded. However, because this control gradually settles to a new attitude of the joint spacecraft system rather than abruptly turning off at a future time, there is no second spike as was observed with the orbital maneuver. In addition, at increasing values of α, the constraint violations exhibit less high-frequency noise after the maneuver is applied because the noise is dampened by the control torque keeping the spacecraft system in a fixed attitude. Moreover, similar to the orbital maneuver, the post-orbital maneuver steady-state constraint violation doesn't settle to the pre-orbital maneuver levels in all cases.

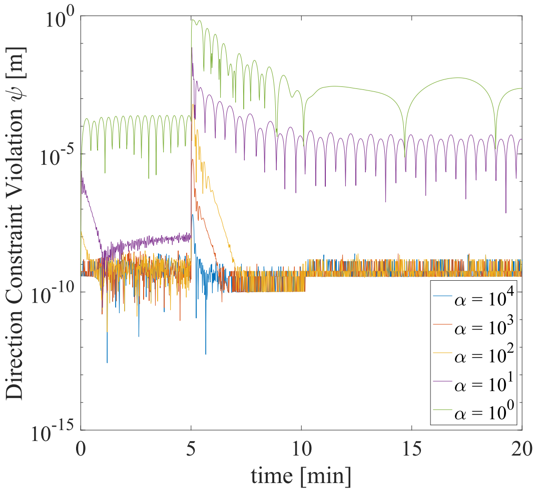

Figure 15: Rigid constraint direction violations with attitude maneuver.

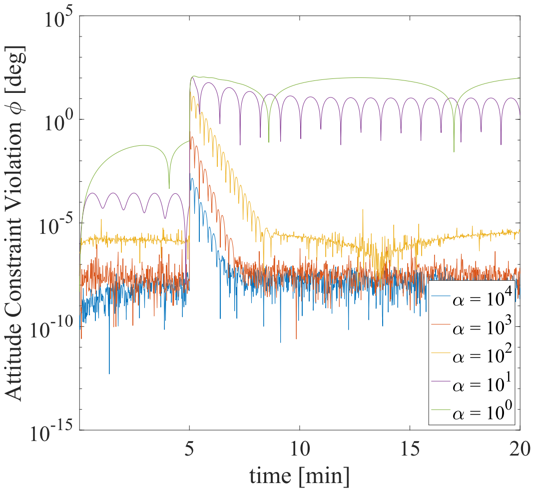

Figure 16: Rigid constraint attitude violations with attitude maneuver.

A plot of each spacecraft's attitude expressed in modified Rodrigues parameter components during the rotational maneuver is shown in Figure 17 from the run using $\alpha = 10^2$. The dashed lines show the attitude of spacecraft 2, which has the same settling time as that of spacecraft 1 in solid lines. Despite this behavior, spacecraft 2 has a more significant overshoot and oscillations in attitude caused by its lagging behind spacecraft 1. This lag occurs because the maneuver torque is applied exclusively to spacecraft 1 and only passed on to spacecraft 2 through the attitude constraint force. Nonetheless, both spacecraft settle to the intended reference attitude despite the attitude control being only directly applied to spacecraft 1, confirming that they are translationally and rotationally locked together.

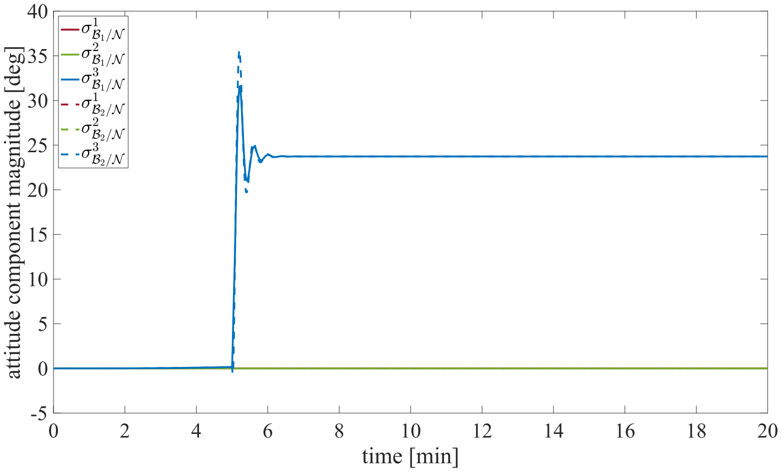

Figure 17: Attitude for both spacecraft with the rotational maneuver.

Complex Spacecraft Model Analysis

With the constraint method validated in Matlab using simplified spacecraft models, the final analysis utilizes the Basilisk Simulation Framework, a flight-proven modular mission simulation framework, to implement a high-fidelity simulation. It is therefore used to introduce pre-existing models of onboard components to each spacecraft that affect its dynamics, stress-testing the constraint method. The software implementation of this open-source architecture and all example scenarios are available online from the Basilisk web site*.

First, the same scenarios explored in the PD gain analysis section are generated in Basilisk with the componentless simplified spacecraft and found to match the results from in Matlab. This process reveals the importance of sub-integration timestep sequencing when using this constraint method in any simulation framework. Basilisk defaults to integrating the equations of motion for a spacecraft, along with the connected state effectors, in a sequential manner across a timestep rather than in a parallel manner. However, with the docking dynamics it is critical that all docked spacecraft dynamics are integrated simultaneously. Otherwise at orbital speeds when integrating the position of the spacecraft to a future timestep, this would put the spacecraft being integrated significantly far away from its attached spacecraft that isn't simultaneously being integrated resulting in wildly inaccurate constraint violations. Therefore, Basilisk 2.2.0 onwards allows the integration of multiple spacecraft systems to be fully coupled to yield synchronized integration of the equations of motion across the timestep.

Solar Panels Observing that the perturbations from the reaction wheel jitter are small enough to have a negligible effect on the constraint introduces the question of how larger perturbations affect the constraint. To investigate larger perturbations, the next component introduced is a flexible solar panel. In this case, a single solar panel is introduced to both spacecraft in the configuration shown in Figure 18. At 10 seconds into the simulation, the solar panel on the servicer spacecraft (B_1) is changed from at rest to have a positive angular velocity with respect to the $\mathcal{B}_1$ frame. The constraint violations for this scenario are shown in Figure 19 There is a spike in constraint violations in both the direction constraint and attitude constraint at 10 seconds when the perturbation is introduced, but the violations are still kept to small orders of magnitude. To further evaluate the effectiveness of the constraint, a "truth" model spacecraft is used to compare the resulting motion of the solar panels. The truth model spacecraft is a single model with the combined inertia properties of the

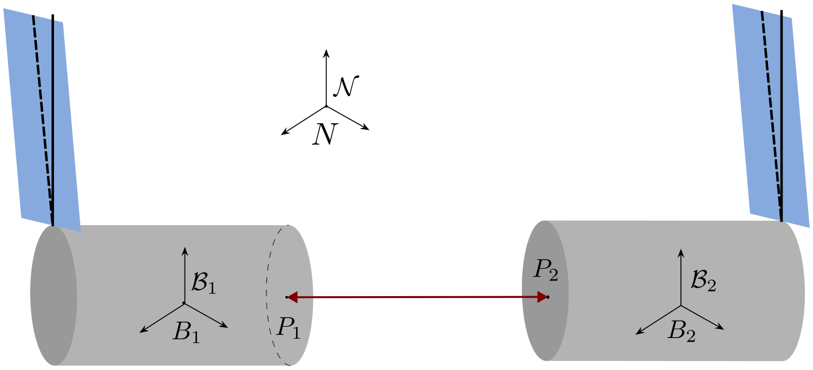

Figure 18: Solar panel configuration.

---

*http://hanspeterschaub.info/basilisk/index.html

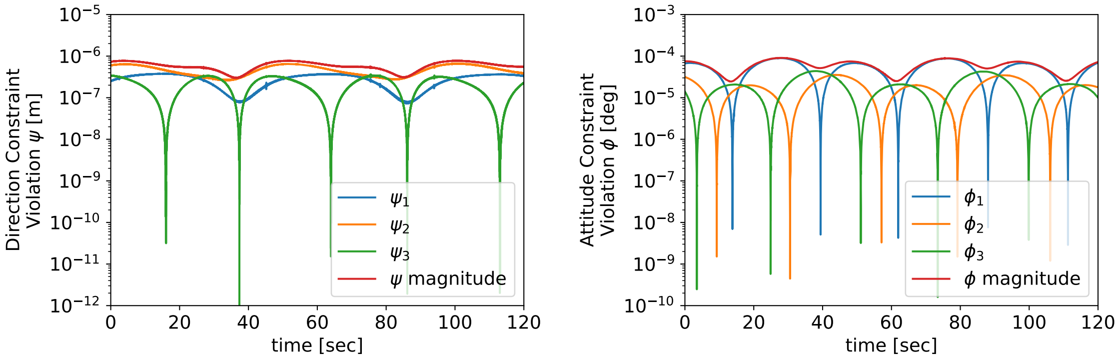

(a) Direction Constraint

(b) Attitude Constraint

Figure 19: Rigid constraint violations with perturbed solar panels.

two-spacecraft-system connected by a constraint. The resulting angle history of both solar panels is shown in Figure 20 with solid lines representing the displacement using the two spacecraft constrained model and the dashed lines representing the displacement using the single spacecraft model. The settling time of the solar panels is shorter when the constraint is used compared to the single spacecraft model, showing that the constraint adds damping to the whole structure that affects the panels. This is further confirmed by setting the damping factor on each panel to zero and showing that the panels come to rest over a long time span with the constraint in effect. However, a panel with no damping is unrealistic, and the damping effects of the constraint can be rather small compared to the natural damping effects when the constraint is stiff.

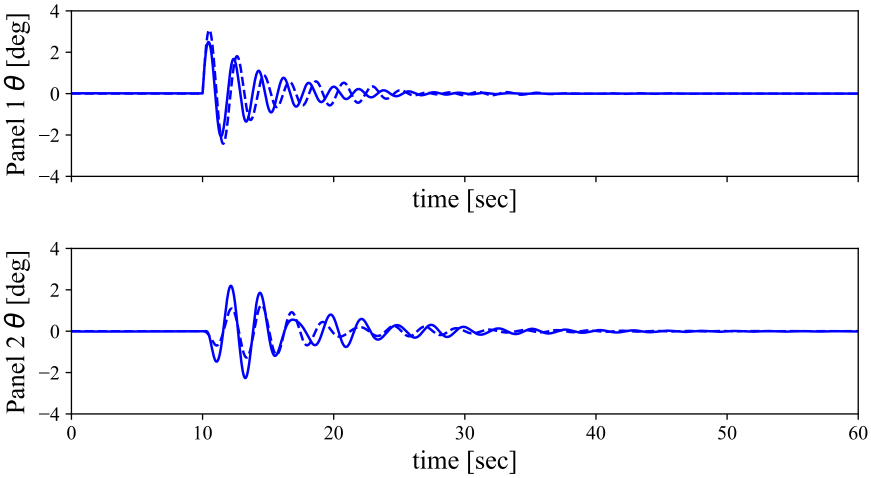

Figure 20: Solar panel angles history.

Fuel Tank The third component introduced is fuel tanks with slosh modeling. Considering that one of the primary motivators of on-orbit servicing missions is refueling, there is potential for servicing vehicles to have a significant mass fraction that is fuel. For this scenario a fuel tank is added only to the servicer spacecraft assuming that the target spacecraft has run out or is very low on fuel. At 10 seconds into the simulation, the at rest fuel is excited with velocities added in all three axes. The resulting constraint violations are shown in Figure 21. As expected, the constraint violations have a sharp increase when the perturbation is introduced, but eventually settle to the same order of magnitude as before the perturbation. Similarly to the solar panel scenario, a truth spacecraft model is used to compare the sloshing motion between the two-spacecraft-constrained model and the single spacecraft model. The resulting slosh motion in all three axes is shown in Figure 22 with solid lines representing the displacement using the two spacecraft constrained model and the dashed lines representing the displacement using the single spacecraft model. The slosh displacements are shown to be nearly identical, and their settling time scale matches the settling on constraint violations.

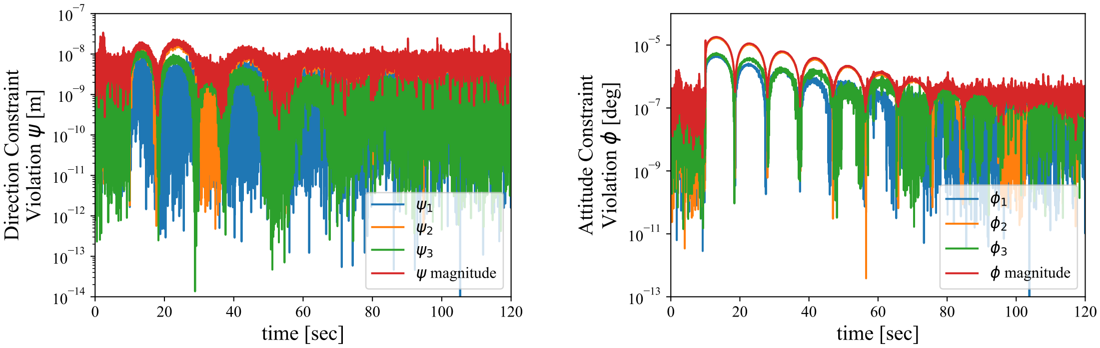

(a) Direction Constraint

(b) Attitude Constraint

Figure 21: Rigid constraint violations with fuel slosh.

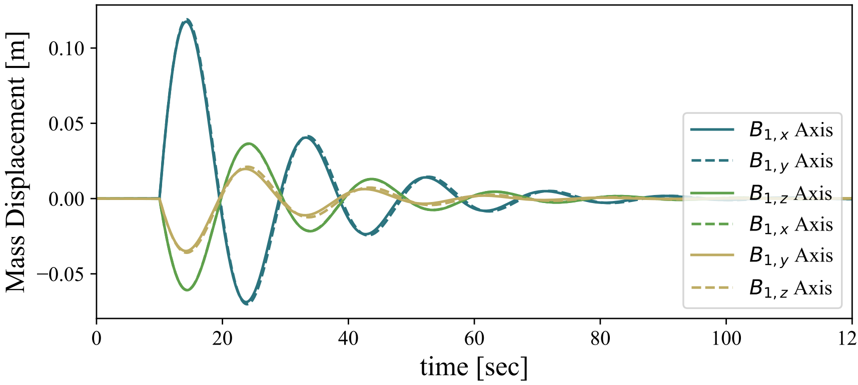

Figure 22: Slosh displacement history.

The cause for the solar panel and slosh component comparisons being near identical but not exact results from residual spacecraft angular rates in the constraint model that do not exist in the single spacecraft model. These angular velocities are excited by the constraint at the start of the simulation with uncertain cause. Even in initial configurations with both spacecraft and their components at rest, the constraint produces a large torque that excites the spacecraft's angular velocities within the first second. The constraint eventually drives these spacecraft angular velocities back to zero, but some small residual angular velocity is left that slightly changes the effects of the solar panel or fuel when they are manually excited later in the simulation. The initial excitation at the simulation startup does not occur when there are no components attached to the spacecraft. The initial excitation at simulation startup is recognized as an issue in the constraint effector's performance, and investigation into its removal is a topic of future work.

In each of these complex spacecraft model analyses, the use of variable timestep integrators is crucial for optimizing simulation runtime. The variable timestep allows the simulation to reduce its timestep drastically as dynamic perturbations are introduced, and then increase the timestep once the system has again settled out. Often this sub-integration timestep is reduced by several orders of magnitude at the first introduction of a perturbation such as exciting the solar panel on the servicer spacecraft.

CONCLUSION AND FUTURE WORK

With spacecraft docking becoming increasingly significant in recent decades and even more interest on the horizon, correctly simulating spacecraft in this scenario is essential to guarantee that mission objectives are met. This work provides a numerical approach to this problem, which aims to facilitate ease of early prototyping and mission analysis.

An analytical mathematical formulation is provided for the Bamgarte stabilization method to enforce the holonomic constraints of the system. The general problem is formulated to be general and applicable to different scenarios involving docked spacecraft. Multiple constraints are explored with increased rigidity to guarantee that the approach is sound for more complex, rigid, and increasingly realistic situations.

Gain selection is an essential element of the Baumgarte stabilization method, as it determines the performance and efficiency of the approach. The PD gain analysis shows that choosing increasingly more significant gains improves performance at the cost of runtime until the results plateau. The PID formulation yields an order-of-magnitude better performance than the PD formulation with the same runtime.

With the constraint method validated against each of these component types, the advantage of enforcing docking constraints without having to re-derive problem-specific system equations of motion is fully realized. This makes the constraint method especially convenient for early mission design when trades are being made on including different spacecraft components, their configurations, and/or how many instances to include. While the constraint method provides ease in changing spacecraft components, it does not provide a free lunch. With the addition, removal, or parameter change of each component on each spacecraft, the α and β gains for both the direction and attitude constraints may need to be reconsidered to ensure that the constraint violations are kept within desirable levels.

Overall, the Baumgarte stabilization method has proved to be an effective way to simulate docking-constrained spacecraft dynamics. The proper gain selection can accurately describe the behavior of the post-docked dynamics of two spacecraft in various scenarios and component configurations. This includes everything from coasting to orbital and attitude maneuvers and from simple spacecraft to complex reaction wheels, solar panels, and fuel tanks.

ACKNOWLEDGMENT

Part of this research was supported through the Space Force STTR Phase I project in collaboration with Starfish Space.

REFERENCES

[1] A. Ellery, J. Kreisel, and B. Sommer, "The case for robotic on-orbit servicing of spacecraft: Spacecraft reliability is a myth," *Acta Astronautica*, Vol. 63, No. 5-6, 2008, pp. 632–648.

[2] R. L. Newman, "STS-61 mission director's post-mission report," tech. rep., 1995.

[3] N. T. Redd, "Bringing satellites back from THE DEAD: Mission extension vehicles give defunct spacecraft a new lease on life," *IEEE Spectrum*, Vol. 57, 2020, pp. 6–7.

[4] M. A. Shoemaker, M. Vavrina, D. E. Gaylor, R. Mcintosh, M. Volle, and J. Jacobsohn, "OSAM-1 decommissioning orbit design," *AAS/AIAA Astrodynamics Specialis t Conference*, 2020.

[5] B. B. Reed, R. C. Smith, B. J. Naasz, J. F. Pellegrino, and C. E. Bacon, "The restore-L servicing mission," *AIAA space 2016*, p. 5478, 2016.

[6] ESA, "ESA Purchases World-First Debris Removal Mission From Start-Up," January 2020.

[7] OrbitFab, "Rapidly Attachable Fluid Transfer Interface Technical Datasheet," `https://catalog.orbitaltransports.com/content/brands/orbitfab/RAFTIBrochure.pdf`, 2022.

[8] A. Rivolta, P. Lunghi, and M. Lavagna, "GNC & robotics for on orbit servicing with simulated vision in the loop," *Acta Astronautica*, Vol. 162, 2019, pp. 327–335, https://doi.org/10.1016/j.actaastro.2019.06.005.

[9] T. Rybus and K. Seweryn, "Manipulator trajectories during orbital servicing mission: numerical simulations and experiments on microgravity simulator," *Progress in Flight Dynamics, Guidance, Navigation, and Control–Volume 10*, Vol. 10, 2018, pp. 239–264.

[10] J. Baumgarte, "Stabilization of constraints and integrals of motion in dynamical systems," *Computer Methods in Applied Mechanics and Engineering*, Vol. 1, No. 1, 1972, pp. 1–16, https://doi.org/10.1016/0045-7825(72)90018-7.

[11] P. Flores, M. Machado, E. Seabra, and M. T. d. Silva, "A parametric study on the Baumgarte stabilization method for forward dynamics of constrained multibody systems," *Journal of computational and nonlinear dynamics*, Vol. 6, No. 1, 2011.

[12] U. M. Ascher, H. Chin, L. R. Petzold, and S. Reich, "Stabilization of constrained mechanical systems with daes and invariant manifolds," *Journal of Structural Mechanics*, Vol. 23, No. 2, 1995, pp. 135–157.

[13] B. Chen and Y. Geng, "Simulation of rendezvous and docking between service spacecraft and non-cooperative target with MATLAB-Simulink and STK," *Proceeding of the 11th World Congress on Intelligent Control and Automation*, IEEE, 2014, pp. 5727–5732.

[14] P. W. Kenneally, S. Piggott, and H. Schaub, "Basilisk: A Flexible, Scalable and Modular Astrodynamics Simulation Framework," *Journal of Aerospace Information Systems*, Vol. 17, Sept. 2020, pp. 496–507.

[15] C. Allard, M. Diaz-Ramos, P. W. Kenneally, H. Schaub, and S. Piggott, "Modular Software Architecture for Fully-Coupled Spacecraft Simulations," *Journal of Aerospace Information Systems*, Vol. 15, No. 12, 2018, pp. 670–683, 10.2514/1.I010653.

[16] J. Alcorn, C. Allard, and H. Schaub, "Fully Coupled Reaction Wheel Static and Dynamic Imbalance for Spacecraft Jitter Modeling," *AIAA Journal of Guidance, Control, and Dynamics*, Vol. 41, No. 6, 2018, pp. 1380–1388, 10.2514/1.G003277.

[17] J. V. Carneiro and H. Schaub, "Novel Architecture for Numerical Multi-satellite Simulations," *International Workshop on Satellite Constellations and Formation Flying*, Milano, Itlay, June 7–10 2022.